Modeling wetting-phase relative permeability hysteresis based on subphase evolution

Comput Geosci (2017) 21:863–875
DOI 10.1007/s10596-017-9655-y

ORIGINAL PAPER

Modeling wetting-phase relative permeability hysteresis based on subphase evolution

Karim Khayrat[1] · **Patrick Jenny**[1]

Received: 30 September 2016 / Accepted: 21 April 2017 / Published online: 24 May 2017

Abstract A recently introduced subphase framework for modeling the nonwetting phase relative permeability is extended to the wetting phase. Within this framework, the wetting phase is divided into four subphases, which are distinguished by their connectivity; backbone, dendritic, isolated and corner-film subphases. The subphase saturations evolve according to inter-subphase volume transfer terms, which require modeling. An advantage of distinguishing the subphases is that wetting phase relative permeability relations as functions of these constituent subphases can be developed. In order to develop models for the inter-subphase volume transfer and the wetting phase relative permeability in a strongly wetted system, quasi-static flow simulations in pore networks were conducted to analyze the evolution of the wetting subphases during drainage and imbibition. The simulation results suggest that hysteresis trends apparent in experimentally obtained wetting phase relative permeability curves for Berea sandstone may be explained by accounting for corner-film flow.

Keywords Relative permeability · Hysteresis · Porous media · Two-phase flow

1 Introduction

Modeling two-phase flow in porous media is important for a large number of applications including carbon dioxide sequestration and enhanced oil recovery. The basis for many macroscopic models describing two-phase flow through porous media is Darcy's law, in which relative permeabilities are important parameters. These quantify the conductance of a porous medium for the two different phases.

In principle, the relative permeabilities are functions of the spatial fluid-phase arrangement. Nevertheless, the relative permeabilities are usually modeled as functions of fluid saturations only, as these have been traditionally readily measured in experiments. However, the relationship between the relative permeabilities and fluid saturations exhibits hysteresis, and hence requires nontrivial models.

Several existing nonwetting-phase relative permeability hysteresis models assume that hysteresis is caused by trapping of the nonwetting phase during imbibition [13, 28, 29]. However, such models do not qualitatively capture the hysteretic behavior of the nonwetting-phase relative permeability for some media. Furthermore, although experimentally obtained wetting-phase relative permeabilities exhibit hysteresis [1, 6, 33], they are usually assumed to be non-hysteretic functions of saturation. In order to understand the causes for the observed hysteresis, pore-scale information is required.

Pore-scale information may be obtained either through numerical simulations or experiments. Numerical simulation methods, such as volume of fluid (VOF) methods [21, 35, 42], lattice Boltzmann methods [17, 31] and pore network models [10, 16, 34] have been widely used to study two phase flow in porous media. Of the three methods, pore network models are the cheapest computationally. They have been used to investigate a wide variety of phenomena such as the effect of pore-structure on relative permeability (e.g., [2, 3, 9, 11, 23]); the relationship between capillary pressure and fluid-fluid interfacial area [24, 25, 37]; the effect of inertia on interface displacement patterns [32]; and ganglion dynamics [14, 15, 43]. An advantage of

✉ Karim Khayrat
khayratk@ifd.mavt.ethz.ch

[1] ETH Zurich, Zurich, Switzerland

pore-network simulations compared to experiments is that one can isolate and study the effects of several microscale properties, such as pore size distribution, flow rates, and contact angle hysteresis on the macroscale flow properties such as relative permeability.

Recently, a large number of experiments have been conducted in which two-phase flow processes in porous media are imaged using X-ray computed micro-tomography. This has made a vast amount of pore-scale data available such as the Euler characteristic [18], interfacial surface area [39] and ganglion size distribution [8]. However, current Darcy-scale models typically do not incorporate such information, but rather rely on empirical relations between the saturation and macroscopic quantities such as relative permeabilities and capillary pressure. In this paper, a model for the wetting phase relative permeability will be proposed based on pore-scale observations obtained through pore network simulations.

In a previous theoretical work presented by Hilfer [19], the nonwetting and wetting fluid phases is each divided into a continuous hydraulically connected subphase and a trapped nonpercolating subphase. Hysteretic relations for relative permeabilities and capillary pressure were developed based on this division. Building on this work, a subphase modeling framework was recently devised by Khayrat and Jenny [27], where the connected nonwetting-phase is further divided into backbone and dendritic subphases. Pore-network simulations were used to study the evolution of the subphases in the context of modeling the nonwetting phase relative permeability. A nonwetting-phase relative permeability model as a function of the backbone subphase was proposed which captured complex hysteretic behavior.

Here, the subphase modeling framework is extended to the wetting phase with the wetting phase sub-divided into backbone, dendritic, film, and isolated subphases. In Section 2, the wetting subphases are defined and their evolution equations are presented. The evolution equations contain volume transfer terms which require modeling. For this purpose, experimental data is required. Due to the difficulty in obtaining such data, quasi-static pore-network simulations are employed as a substitute for experiments. Simulation results for the evolution of the wetting subphases as well as for the wetting-phase relative permeability are discussed in Section 3. Next, in Section 4, insights gained from flow simulations in pore-network are used to propose a model for the wetting-phase relative permeability in terms of the subphase saturations.

2 Theory

In this paper, incompressible immiscible two-phase flow in a rigid porous medium is considered, where one fluid is nonwetting and the other is wetting. The receding and advancing contact angles are assumed to be zero, i.e., strongly wetting conditions are assumed. Furthermore, sufficiently low capillary numbers are assumed such that viscous effects can be neglected. Let S_n and S_w denote the nonwetting and wetting-phase saturations, respectively. The mass conservation equations of the wetting and nonwetting phases can be written as [5]

$$\phi \frac{\partial S_\alpha}{\partial t} - \frac{\partial}{\partial x_i}\left(\frac{K}{\mu_\alpha} k_{r\alpha} \frac{\partial P_\alpha}{\partial x_i}\right) = 0, \tag{1}$$

where Darcy's law for two-phase flow is assumed and gravity is neglected. Here, ϕ is the porosity of the porous medium, K the absolute permeability, and P_α, μ_α and $k_{r\alpha}$ the pressure, viscosity and relative permeability of phase α, respectively, where $\alpha = n$ denotes the nonwetting and $\alpha = w$ the wetting phase. The nonwetting and wetting pressures are related by the macroscopic capillary pressure

$$P_c(S) = P_n - P_w. \tag{2}$$

For simplicity, throughout this paper, the wetting and nonwetting saturations should be interpreted as scaled saturations, related to the actual phase saturation $\overline{S_\alpha}$ by the relation

$$S_\alpha = \frac{\overline{S_\alpha} - \overline{S_{w_{IR}}}}{1 - \overline{S_{w_{IR}}}}, \tag{3}$$

where $\overline{S_{w_{IR}}}$ is the connate (or irreducible) wetting saturation.

2.1 Wetting fluid subphases

The wetting phase can be divided into four separate subphases: a backbone subphase, a dendritic subphase, a film subphase, and an isolated subphase (see Fig. 1a). The total wetting-phase saturation can be written as

$$S_w = S_{wb} + S_{wd} + S_{wi} + S_{wf}, \tag{4}$$

where the subscripts b, d, i and f identify the backbone, dendritic, isolated and film subphases, respectively.

In order to define the subphases, the porous medium is assumed to be represented by a network consisted of pore-bodies and pore-throats. A representative elementary volume (REV) [5] of the porous medium is then considered, which is large enough such that the subphase saturations are independent of the REV size. The wetting backbone subphase consists of the volume of wetting-phase-filled (WPF) pores which can be connected to both inlet and outlet boundaries of the REV by at least two independent simple paths through WPF pores. Two paths are independent if they do not share a pore-throat. The wetting dendritic subphase

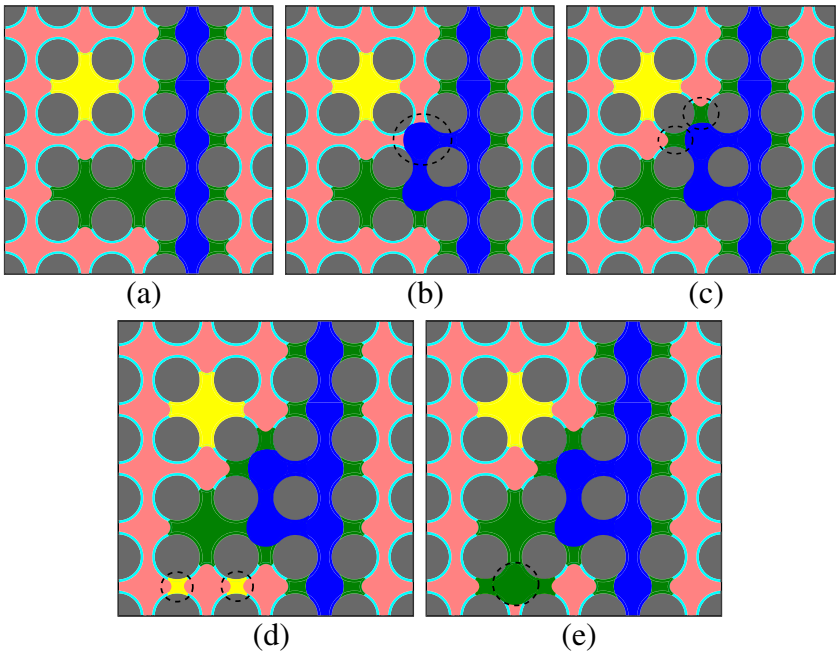

Fig. 1 Conceptual illustration of the wetting backbone (*dark blue*), dendritic (*green*), film (*light blue*) and isolated (*yellow*) subphases during imbibition. The *gray* and *red regions* represent the solid and nonwetting phase, respectively. The *dashed ellipses* highlight changes in the fluid-fluid interface. The flow direction is from *bottom* to *top*. Note that the illustration represents a two-dimensional slice of a porous medium and that all the volume belonging to the film subphase is connected through the wetting phase in three dimensions. **a** Hypothetical fluid distribution at the beginning of imbibition. **b** Increase in the backbone subphase saturation after a cooperative pore-filling event and the resulting transfer of dendritic and film subphase volumes to the backbone subphase volume. **c** Increase in the dendritic subphase saturation after piston displacement events and the resulting transfer of film subphase volume to the dendritic subphase volume. **d** Increase in the isolated subphase saturation after snap-off displacement events and the resulting transfer of film subphase volume to the isolated subphase volume. **e** Increase in the dendritic subphase saturation after a cooperative pore-filling event and the resulting transfer of isolated and film subphase volume to the dendritic subphase volume

consists of the volume of WPF pores which can be connected to the REV boundary by only one independent path through WPF pores. The wetting isolated subphase consists of WPF pore-volumes surrounded by NPF pores.

The film subphase consists of the volume of thin wetting films covering the solid surface as well as thicker films in the corners of nonwetting-phase-filled (NPF) pores. The thin wetting films are typically a few nanometers thick [41], and their contribution to the saturation is neglected here. On the other hand, the volume of the corner films are non-negligible [40] and taking them into account is important in correctly predicting the wetting-phase relative permeability [10]. Note that under strong wettability conditions, the wetting phase forms a connected phase even at low wetting-phase saturation values.

Note that the considered REV is required to satisfy both a lower and an upper bound. The lower bound is required to ensure that the REV is sufficiently large, such that the subphase saturations are independent of the REV size. Such a lower bound may not necessarily exist if the porous medium is heterogeneous at all scales. Furthermore, since we have assumed capillary dominated flow, an upper bound for the REV size is required such that the macroscale capillary pressure $\overline{Ca}$ and macroscopic gravillary number $\overline{Gl}$ [20] are negligibly small. This ensures that the viscous pressure drop and gravitational pressure drop across the REV are negligible compared to the capillary pressure, and hence capillary equilibrium within the REV can be assumed.

2.2 Subphase evolution

During imbibition, the wetting-phase saturation increases and the wetting subphase saturations evolve with volume being transferred between the subphases. An increase in the wetting-phase saturation can result in a direct increase in the wetting backbone due to a cooperative pore-filling displacement and a resulting transfer of dendritic and film subphase volumes to the backbone subphase (Fig. 1a, b). Here, "direct" indicates that the volume previously occupied by the nonwetting phase is transferred to a particular wetting subphase after a displacement event without initially being transferred to another subphase.

A direct increase in the dendritic saturation can occur either due to piston-type displacements (Fig. 1b, c), resulting

in volume transfer from the film to the dendritic subphase, or due to cooperative pore-filling displacement (Fig. 1d, e), resulting in volume transfer from the film (and possibly the isolated) subphase to the dendritic subphase. A direct increase in the isolated subphase can occur due to snap-off displacement (Fig. 1c, d), resulting in volume transfer from the film subphase to the isolated subphase. It can also occur due to cooperative pore-filling and piston-type displacements. Finally, a direct increase in the film subphase saturation is caused by swelling of wetting film as the capillary pressure decreases during imbibition. This swelling can only occur in pore-bodies occupied by the connected non-wetting subphase due to the assumed incompressibility.

Similarly, during drainage, the wetting phase decreases, which results in a direct decrease in the wetting subphases, as well as volume transfer between the subphases. Furthermore, the nonwetting phase displaces the wetting phase only through piston-type displacements, leading to different fluid phase arrangements in the porous medium than during imbibition. This in turn results, for drainage-imbibition cycles, in the non-uniqueness of the relative permeabilities as a function of the fluid saturations. Modeling the evolution of the subphase evolution would allow to develop relative permeability models which take into account the contributions of the different subphases.

The evolution of the wetting subphase saturations can be described by

$$\phi \frac{\partial S_{wb}}{\partial t} = \lambda_{wb}\phi \frac{\partial S_w}{\partial t} + Q_{wd-wb} - Q_{wb-wf}, \quad (5)$$

$$\phi \frac{\partial S_{wd}}{\partial t} = \lambda_{wd}\phi \frac{\partial S_w}{\partial t} - Q_{wd-wi} - Q_{wd-wb} - Q_{wd-wf}, \quad (6)$$

$$\phi \frac{\partial S_{wi}}{\partial t} = \lambda_{wt}\phi \frac{\partial S_w}{\partial t} + Q_{wd-wi} - Q_{wi-wf} \quad (7)$$

and

$$\phi \frac{\partial S_{wf}}{\partial t} = \lambda_{wf}\phi \frac{\partial S_w}{\partial t} + Q_{wb-wf} + Q_{wd-wf} + Q_{wi-wf}, \quad (8)$$

where $Q_{\beta_1-\beta_2}$ is the volume transfer between subphases β_1 and β_2, and $\lambda_{wb}, \lambda_{wd}, \lambda_{wf}, \lambda_{wt} \in [0, 1]$ with $\lambda_{wb} + \lambda_{wd} + \lambda_{wf} + \lambda_{wt} = 1$. The terms of the form $\lambda_\beta \phi \frac{\partial S_w}{\partial t}$ indicate the direct increase in subphase β. Note the absence of a term capturing the volume transfer between the backbone and isolated wetting subphases Q_{wb-wi}. Under the assumption that only one pore scale event may occur instantaneously, during imbibition a volume of isolated wetting phase is transferred to the dendritic subphase first and can only become part of the backbone subphase when another fluid path is established after further imbibition. In order to provide relations for $Q_{\beta_1-\beta_2}$ and λ_β, pore-scale information is required.

3 Pore network study

In order to study the wetting subphase saturations as well as the wetting-phase relative permeability (WRP), pore-network models are employed. Note that it is not our aim here to compare experimental data which pore-network simulation results. Rather we consider pore-network simulations as substitutes for real experiments and rely on their qualitative behavior being correct. However, provided sufficient data are available, a similar analysis could be conducted based on laboratory experiments.

3.1 Network models

Two structured pore-network models, representing artificial consolidated (network A) and unconsolidated (network B) porous media, as well as one unstructured pore-network representative of Berea sandstone (network C), are employed in this work. The structured networks consist of 120 × 60 × 60 pore bodies (120 pore bodies along the general flow direction) with each pore body having 6 incident pore throats. The pore elements (i.e., pore throats and pore bodies) of networks A and B have square cross-sections with inscribed radii distributed, following [23], according to the beta distribution

$$f(r) = \frac{(r - r_{min})^{a-1}\,(r_{max} - r)^{b-1}}{(r_{max} - r_{min})^{a+b-1}\,B(a, b)}, \quad (9)$$

where a and b are shape parameters, r_{min} and r_{max} are the minimum and maximum inscribed radii, respectively, and $B(a, b)$ is the beta function. The parameters used are given in Table 1. Network C was generated by the stochastic pore network generator described by [22] and consists of 670,000 pore-bodies and 1.4 million pore-throats, each having a cross-section characterized by a different shape-factor

$$G = \frac{A_{tot}}{\mathrm{P}^2}, \quad (10)$$

where P and A_{tot} are the cross-sectional perimeter and area of the pore element, respectively. The statistics of network C is shown in Table 2. All networks used here are homogeneous and isotropic.

Table 1 Parameters of beta distribution, Eq. (9), used to sample the pore-elements for the artificial structured pore-networks [23]

	Consolidated		Unconsolidated	
	Bodies	Throats	Bodies	Throats
a	1.25	1.5	2.5	1.5
b	2.5	2	1.5	1.5
$r_{\min}$ (μm)	20	1	40	15
$r_{\max}$ (μm)	75	25	64	40

Table 2 Pore size statistics of network C, generated by the stochastic pore network generator described in [22]

	Maximum	Minimum	Mean	Standard deviation
Inscribed pore-body radius (μm)	73.5	3.62	19.3	8.44
Inscribed pore-throat radius (μm)	48.7	0.90	10.4	6.37
Coordination number	19	2	4.14	1.43
Number of pore bodies	$0.67E6$			
Number of pore throats	$1.41E6$			
Network size (cm^3)	$1.8 \times 0.9 \times 0.9$			

3.2 Simulation of drainage and imbibition

In this subsection, the simulation of drainage and imbibition in a pore-network are briefly described and the treatment largely follows [34]. The implementation details for the drainage and imbibition algorithms can be found in [26, Appendix C].

In order to simulate both primary and secondary drainage, an algorithm essentially identical to the standard invasion percolation algorithm [44] is employed and consists of successive piston-type pore displacements. At each step, the WPF pore throat or pore body which has the least threshold capillary pressure is invaded by the nonwetting phase. The capillary pressure is set to be equal to the largest threshold capillary pressure overcome. This is repeated until a desired nonwetting saturation is reached or the pore-network is fully drained. Following [34], the threshold capillary pressure p_c^e of a pore element is given by

$$p_c^e = \gamma \frac{1 + 2\sqrt{\pi G}}{r}. \tag{11}$$

Here, r is the inscribed radius of a pore-element, γ is the interfacial tension between the nonwetting and wetting phases.

The simulation of imbibition takes into account, in addition to piston-type displacements, snap-off and cooperative pore-body filling events. At each step of the imbibition simulation, the NPF pore throat or pore body which has the greatest threshold capillary pressure is invaded by the wetting phase and the capillary pressure is set to be equal to the least threshold capillary pressure overcome. The threshold capillary pressure for piston-displacement is identical to Eq. (11), while the threshold capillary pressure for snap-off in a pore throat (for zero contact angle) is given by (see [34])

$$p_c^{snapoff} = \frac{\gamma}{r_t}, \tag{12}$$

where r_t is the inscribed radius of pore throat. For cooperative pore filling, the threshold capillary pressure depends on the number of neighboring throats filled with non-wetting fluid [30]. A cooperative pore-filling mechanism of type I_z occurs when z neighboring throats are filled with the nonwetting phase. Following [23], a simple capillary pressure threshold for the I_z displacement mechanism in a pore body of radius r_b is used:

$$p_c^{coop} = \gamma \frac{1 + 2\sqrt{\pi G}}{z r_b}. \tag{13}$$

Note that after a cooperative pore filling mechanism I_z, with $z > 1$, or snap-off has occurred, nonwetting fluid may become trapped. Trapped regions are excluded from further imbibition displacement events. A visualization of the subphase evolution in network C for primary drainage and secondary imbibition is shown in Fig. 2.

3.3 Pore element conductance

In order to compute the relative permeability of the entire network for a given fluid configuration, the conductances of each fluid in a pore element needs to computed. When a pore element (i.e. pore throat or pore body) is filled with nonwetting fluid at the center of the pore and wetting fluid at its corners, the wetting and non-wetting cross-sectional areas are

$$A_w = r_w \left(\frac{1}{4G} - \pi \right), \tag{14}$$

where $r_w = \gamma / P_c$ and

$$A_n = A_{tot} - A_w, \tag{15}$$

respectively [4]. This models the dependence of the corner-film volume on the capillary pressure, which is illustrated in Fig. 3.

The local saturation in a pore element is given by

$$S^{loc} = \frac{A_\alpha}{A_{tot}}, \tag{16}$$

where $\alpha \in \{n, w\}$. Given the local saturation in each pore element, the saturation in the entire network can be obtained for each fluid subphase.

The hydraulic conductance of nonwetting fluid in a pore-element is modeled by (see [4])

$$g_n = \frac{r_{H,n}^2 A_n}{8 \mu_n l}, \tag{17}$$

where l the length of the pore element, μ_n is the viscosity of the nonwetting phase and $r_{H,n} = \frac{1}{2}\left(r + \sqrt{\frac{A_n}{\pi}} \right)$ is the mean

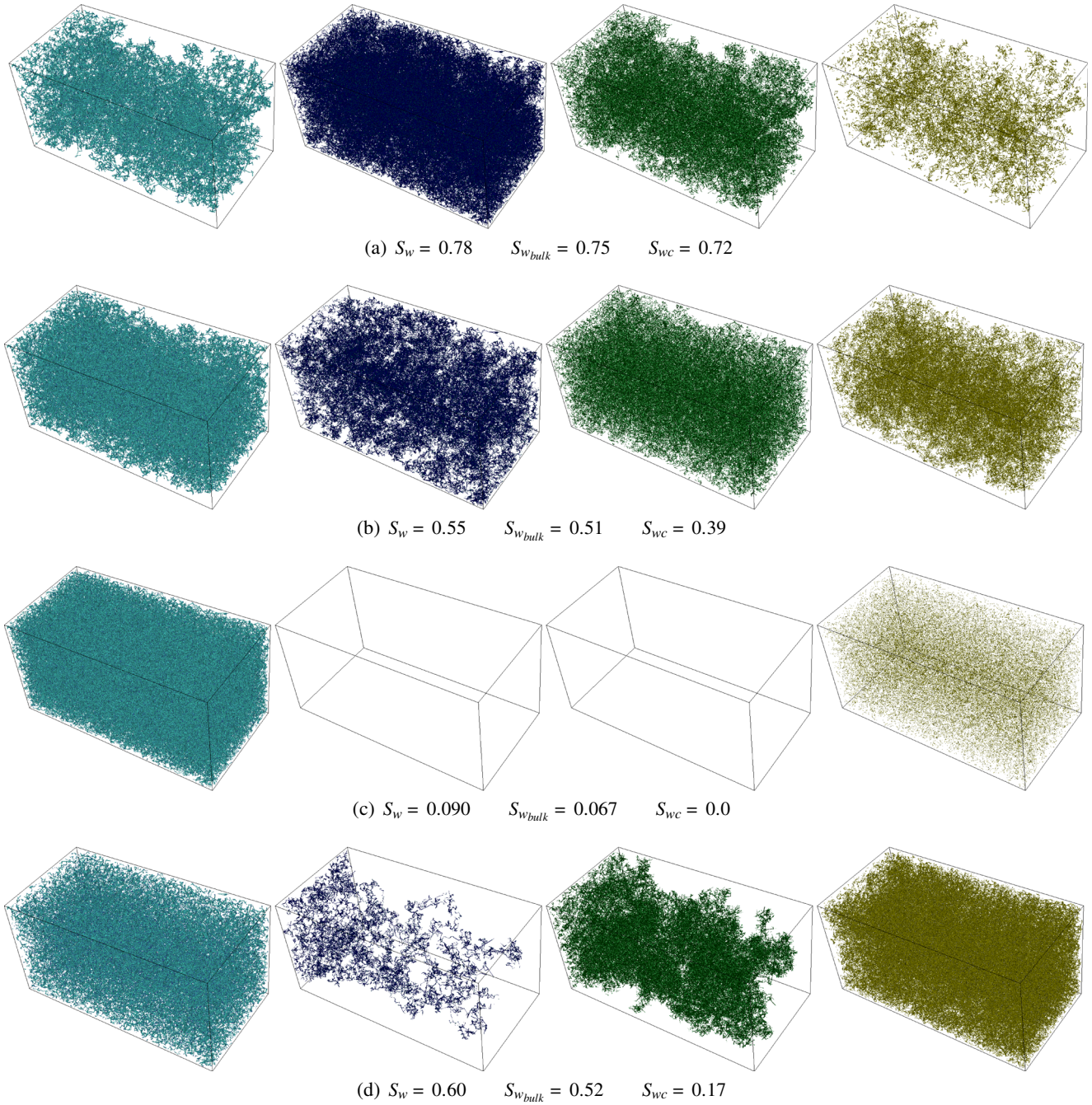

Fig. 2 Structure of the film (*left column*), backbone (*center-left column*), dendritic (*center-right column*) and isolated (*right column*) wetting subphases during a primary drainage-secondary imbibition cycle in network C at four different wetting phase saturations. **a** $S_w = 0.78$ during drainage. **b** $S_w = 0.55$ during drainage. **c** $S_w = 0.09$ during drainage. **d** $S_w = 0.6$ during imbibition. Indicated in all figures are the connected saturation $S_{wc} = S_w - S_{wf}$ and $S_{w_{bulk}} = S_{wb} + S_{wd}$.. Note that the structure of the film subphase as illustrated here is the same as that of nonwetting-phase

hydraulic radius. The hydraulic conductance of the wetting fluid through the corners of a pore element is modeled by

$$g_w = \frac{r_w^2 A_w}{8\beta\mu_w l}, \tag{18}$$

where μ_w is the viscosity of the wetting phase and $\beta = 5.3$ is a dimensionless resistance factor (see [36] for details). When a pore-element is completely filled with wetting fluid, the conductance can be computed as

$$g_w = \frac{r_H^2 A_{tot}}{8\mu_w l}, \tag{19}$$

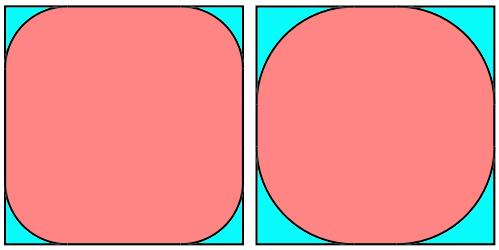

Fig. 3 Wetting corner film (*blue*) and nonwetting fluid (*red*) in a square cross-section of a pore or throat. **a** At a capillary pressure $P_c = P_0$. **b** At a capillary pressure $P_c < P_0$

where $r_H = \frac{1}{2}\left(r + \sqrt{\frac{A_{tot}}{\pi}}\right)$. The effective conductance $g_{\alpha,ij}$ of phase α between the centers of pore i and pore j in a network is computed by the harmonic average

$$\frac{1}{g_{\alpha,ij}} = \frac{1}{g_{\alpha,k}} + \frac{1}{2}\left(\frac{1}{g_{\alpha,i}} + \frac{1}{g_{\alpha,j}}\right), \tag{20}$$

where $g_{\alpha,k}$ is the conductance of the throat connecting pore i and pore j.

3.4 Relative permeability

Given a certain fluid configuration and the corresponding pore element conductances, one can obtain the relative permeabilities by solving for the pressure field in the network with an imposed unit pressure gradient in a given direction and using

$$k_{r\alpha} = \frac{Q^{\alpha}_{tot}\mu_{\alpha}L_{net}}{K A_{net}}, \tag{21}$$

where A_{net} is the network's cross-sectional area orthogonal to the pressure gradient, L_{net} is its length along the pressure gradient, K is the permeability of the network and Q^{α}_{tot} is the across of the network resulting from the applied pressure gradient. Note that an implicit assumption in this procedure is the fluid-fluid interfaces are frozen and the fluid-configuration is homogeneous (see, for example, [12] for more details).

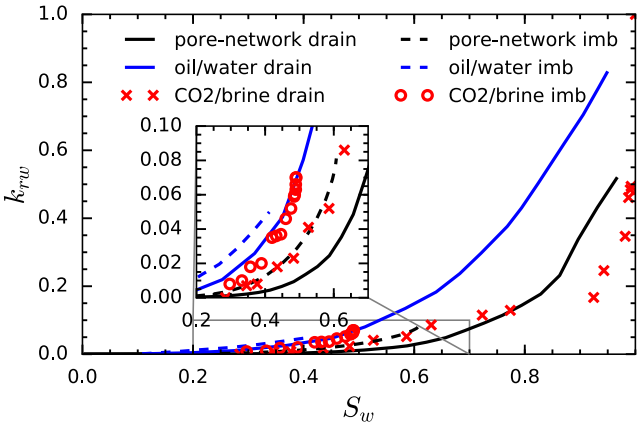

Fig. 5 Primary drainage-secondary imbibition wetting-phase relative permeability curves for Berea Sandstone obtained by pore-network simulations, compared to those obtained experimentally in a supercritical CO_2/brine system (experiment 25 in [1]) and a oil/water system [33] (as presented in [7]). The experimental results are scaled according to Eq. (3) with $\overline{S_{w_{IR}}} = 0.35$ for the CO_2/brine system and $\overline{S_{w_{IR}}} = 0.3$ for the oil/water system

The PD-SI-SD curves of the wetting-phase relative permeability for networks A, B and C are shown in Fig. 4. The wetting-phase relative permeability for all networks is larger during SI than during PD. It can also be observed from Fig. 4 that the WRP for the SI-SD cycle is hysteretic, being larger during SI than during SD. In summary $k^{PD}_{rw} < k^{SD}_{rw} < k^{SI}_{rw}$ for the $k_{rw} - S_w$ relation.

Figure 5 compares the PD and SI wetting phase-relative permeabilities for Network C with experimental measurements by [1] for a supercritical CO_2/brine system in Berea sandstone, and by [33] for an oil/water system in Berea sandstone. There is good qualitative agreement between the network modeling and both of the experimental results. This suggests that the network model employed sufficiently captures the pore-scale mechanisms responsible for WRP hysteresis in strongly wetted systems.

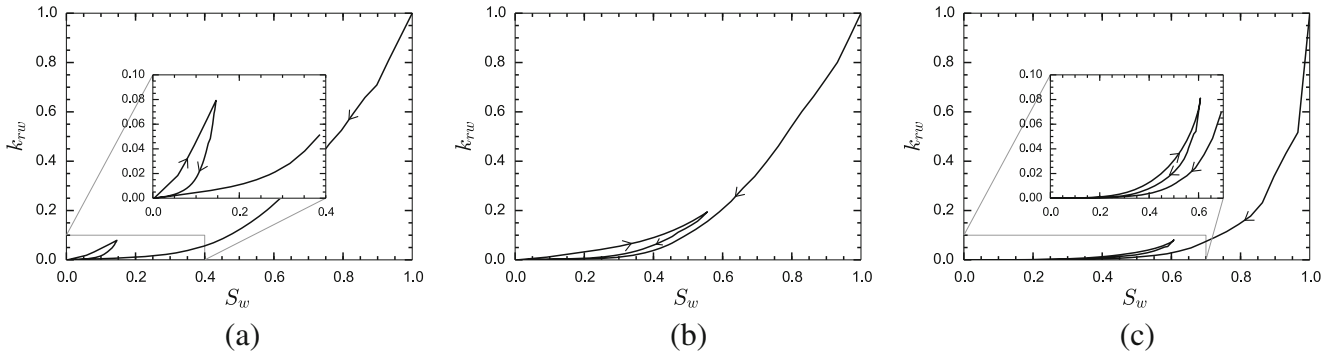

Fig. 4 Pore-network simulation results: PD, SI and SD curves of the wetting-phase relative permeability vs. the wetting-phase saturation for a network representative of (**a**) an artificial consolidated porous medium, (**b**) an artificial unconsolidated porous medium, and (**c**) Berea sandstone

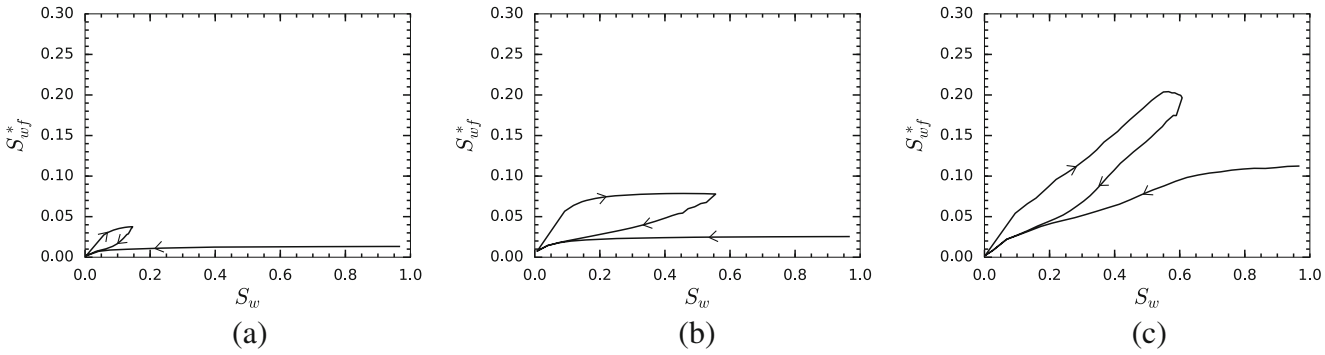

Fig. 6 Pore-network simulation results: PD, SI and SD curves of the normalized film saturation $S^*_{wf} = \frac{S_{wf}}{S_n+S_{wf}}$ vs. the wetting-phase saturation for a network representative of **a** an artificial consolidated porous medium, **b** an artificial unconsolidated porous medium, and **c** Berea sandstone

The quantitative discrepancy between the network modeling results and either of the two experimental results can be attributed to the assumption of a fixed zero advancing and receding contact angle, the simplified geometry and topology used in network models, and the simplified equations used to calculate the phase conductances in each pore element. A better match may be obtained by tuning the network model parameters to fit either of the two experiments.

3.5 Film subphase and capillary pressure

The cause of hysteresis in the $S_w - k_{rw}$ relation can be explained by considering the evolution of the film subphase. Figure 6 shows the evolution of the normalized film saturation $S^*_{wf} = S_{wf}/\left(S_n + S_{wf}\right)$. Note that hysteresis is significant in the S^*_{wf}-S_w relation with $S^{*PD}_{wf} < S^{*SD}_{wf} < S^{*SI}_{wf}$. This is the same trend as observed for the WRP. During drainage, the capillary pressure increases and the wetting film in pores occupied by the connected nonwetting subphase shrinks, while during imbibition the capillary pressure decreases and the wetting film swells in pores occupied by the connected nonwetting subphase. The PD-SI-SD curves of the capillary pressure for the three different networks are shown in Fig. 7.

The behavior of film subphase can account for the hysteresis in S_w-k_{rw} relation as follows: At low wetting-phase saturations, the main bottle-neck for the wetting-phase relative permeability is the wetting film as it has a significantly lower conductance compared to that of the wetting-phase filled pores. Due to film swelling, the conductance of the wetting film is higher during imbibition than during drainage, resulting in the observed hysteresis in the $k_{rw} - S_w$ curves shown in Fig. 4.

3.6 Isolated subphase

Figure 8 shows the PD-SI-SD curves of the isolated wetting subphase saturation S_{wi} vs. the bulk wetting-phase saturation $S_{w_{bulk}} = S_{wb} + S_{wd} + S_{wt}$ for networks A, B and C. During primary drainage, the nonwetting phase displaces and surrounds the wetting phase, causing islands of the wetting phase to become isolated. Below a threshold bulk wetting-phase saturation $S^{crit\,dr}_{w_{bulk}}$, $S_{wi} = S_{w_{bulk}}$ and $S_{wc} = S_{wb} + S_{wd} = 0$. Further drainage results in the draining of the isolated subphase through the wetting film. During imbibition, clusters of isolated wetting phase form through snap-off displacements and these clusters grow through cooperative pore-filling events until, for

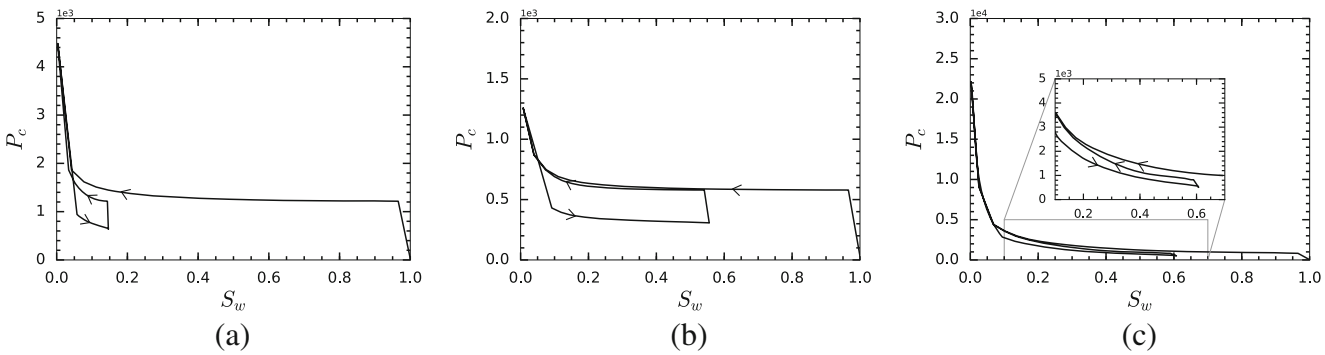

Fig. 7 Pore-network simulation results: PD, SI and SD curves of the capillary pressure vs. the wetting-phase saturation for a network representative of **a** an artificial consolidated porous medium, **b** an artificial unconsolidated porous medium, and **c** Berea sandstone

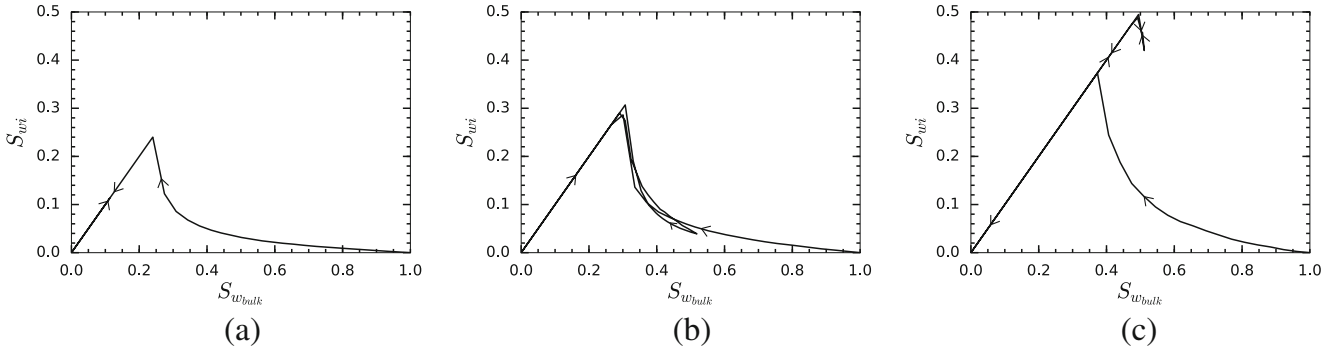

Fig. 8 Pore-network simulation results: PD, SI and SD curves of S_{wi} vs. $S_{w_{bulk}}$ for a network representative of **a** an artificial consolidated porous medium, **b** an artificial unconsolidated porous medium, and **c** Berea sandstone

networks B and C, a threshold bulk wetting-phase saturation $S_{w_{bulk}}^{crit\,imb}$ is reached such that a cluster spanning the network is formed. This threshold is not reached for network A due to significant non-wetting trapping compared to the other two networks. For network B, $S_{w_{bulk}}^{crit\,dr} \approx S_{w_{bulk}}^{crit\,imb}$, while for network C $S_{w_{bulk}}^{crit\,dr} < S_{w_{bulk}}^{crit\,imb}$. Further imbibition results in a decrease in the isolated subphase saturation until the residual nonwetting-phase saturation is reached. Note that no hysteresis is observed in the SI and SD curves of the $S_{w_{bulk}} - S_{wi}$ relation.

3.7 Backbone and dendritic subphases

The PD, SI and SD curves of the subphase saturations S_{wb} and S_{wd} for networks A, B and C are shown in Fig. 9. For network A, $S_{wc} = S_{wb} + S_{wd}$ is nonzero only during primary drainage. Moreover, due to a high $S_{w_{bulk}}^{crit\,imb}$, the range in which $S_{wc} > 0$ is insignificant for network C. For network B, it can be observed that, for a given S_{wc}, $S_{wb}^{SI} < S_{wb}^{SD} < S_{wb}^{PD}$ and $S_{wd}^{PD} < S_{wd}^{SD} < S_{wd}^{SI}$ (see Fig. 9b).

4 Modeling and calibration

In this section, a model for the wetting-phase relative permeability will be proposed and then calibrated using the previously presented network simulation results. It will be shown that the relative permeability may be modeled as a function of the bulk saturation $S_{w_{bulk}}$ and the film saturation S_{wf}. Since the volume transfer terms between the subphases constituting the bulk phase, i.e., Q_{wd-wi} and Q_{wd-wb}, as well as the terms representing their direct change $\lambda_{wd}\phi\frac{\partial S_w}{\partial t}$, $\lambda_{wb}\phi\frac{\partial S_w}{\partial t}$, $\lambda_{wi}\phi\frac{\partial S_w}{\partial t}$, are not required to compute $S_{w_{bulk}}$ and S_{wf}, their modeling will not be pursued here. Models for these terms may be developed in a similar manner as for the volume transfer terms between the backbone, dendritic and trapped nonwetting phase as shown in [27], if required.

For the following, a reduced set of equations

$$\phi\frac{\partial S_{w_{bulk}}}{\partial t} = \left(1-\lambda_{w_{film}}\right)\phi\frac{\partial S_w}{\partial t} - Q_{w_{bulk}-wf}, \tag{22}$$

$$\text{and} \quad \phi\frac{\partial S_{wf}}{\partial t} = \lambda_{w_{film}}\phi\frac{\partial S_w}{\partial t} + Q_{w_{bulk}-wf}, \tag{23}$$

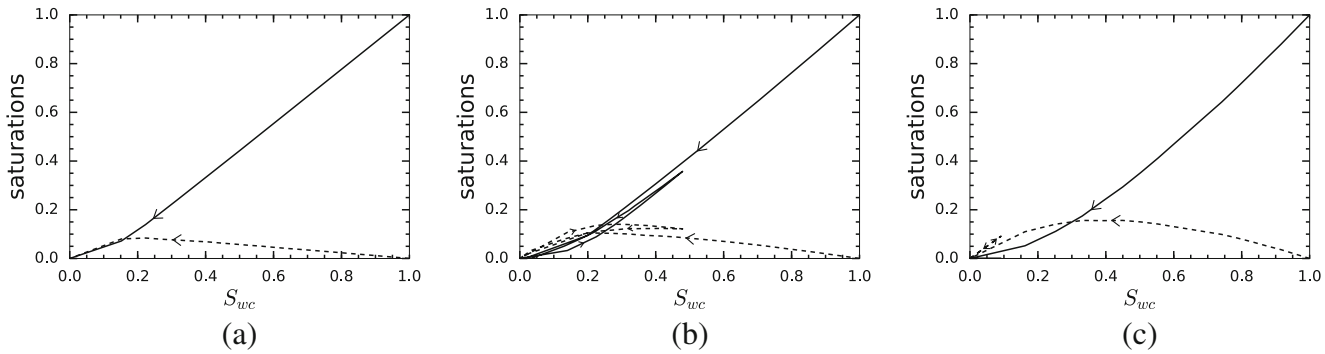

Fig. 9 Pore-network simulation results: PD, SI and SD curves of S_{wb} vs. S_{wc} (solid lines) and S_{wd} vs. S_{wc} (dashed lines) for a network representative of **a** an artificial consolidated porous medium (values are nonzero only for PD curve), **b** an artificial unconsolidated porous medium, and **c** Berea sandstone

which is obtained by summing Eqs. (5–7) and is sufficient for modeling the bulk and film saturations will be considered. Here, $Q_{w_{bulk}-wf} = Q_{wb-wf} + Q_{wd-wf} + Q_{wi-wf}$ is the volume transfer between the bulk and the film wetting subphases, a model of which will be developed in Section 4.2.

4.1 Relative permeability

Contrary to the case of the nonwetting phase described in [27], where the nonwetting-phase relative permeability was determined to be a nearly non-hysteretic function of the nonwetting backbone saturation, the wetting-phase relative permeability is function of all the subphase saturations since they all contribute to the flow. However, it was observed in Figs. 4 and 6 that the hysteresis in the wetting-phase relative permeability may be explained by the swelling and shrinking of the wetting film saturation during imbibition and drainage. Based on this, we propose to model the wetting-phase relative permeability by the relation

$$k_{rw} = \left(\left(1 - S_{w_{bulk}}\right) \left(\frac{S_{wf}}{1 - S_{w_{bulk}}} \right)^{\alpha_w p} + \left(S_{w_{bulk}}\right)^{1+\beta p} \right)^{1/p}, \tag{24}$$

which is a power average of the contribution of the film saturation to the WRP, modeled by $\left(S_{wf}/\left(1 - S_{w_{bulk}}\right)\right)^{\alpha_w}$, and that of the bulk saturation, modeled by $\left(S_{w_{bulk}}\right)^{\beta}$. Note that for $p = 1$ this relation reduces to an arithmetic average, while for $p = -1$ it reduces to a harmonic average. Figure 10 shows a comparison between the wetting-phase relative permeability computed using Eq. (24) for network B and that obtained from pore-network simulations. Note that the values for S_{wf} and $S_{w_{bulk}}$, used to compute the modeled relative permeability, are also obtained from the network simulations. The model is able to capture the hysteretic behavior of the $S_w - k_{rw}$ relation with a good match for the secondary imbibition and secondary drainage curves. However, there is a discrepancy between the model and network results for the primary drainage curve, possibly due to the decrease of the importance of the film subphase saturation for the WRP at higher wetting-phase saturations.

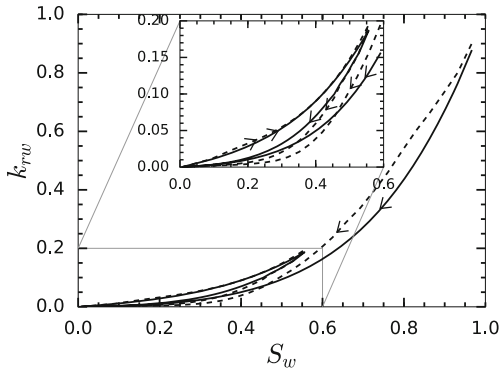

Fig. 10 Comparison between wetting-phase relative permeability curve obtained from the calibrated model Eq. (24) (*solid lines*) and from pore-network simulations (*dashed lines*) for network B. The parameters used in Eq. (24) are $\alpha = 1.7$, $\beta = 0$, $p = 0.18$. The values used for S_{wf} and $S_{w_{bulk}}$ are obtained from the network simulations for network B

4.2 Film saturation

The terms $\lambda_{w_{film}}$ and $Q_{w_{bulk}-wf}$ in Eq. (22), required to compute the film saturation, will now be modeled. It is useful to subdivide the film subphase into two components; one present in the pores occupied by the connected nonwetting phase (which swells or shrinks as the capillary pressure decreases or increases), and another which is present in pores occupied by the trapped nonwetting phase (which due to the assumed incompressibility does not swell or shrink). The saturations of former and latter are denoted in the following as S_{wfc} and S_{wft}, respectively with $S_{wf} = S_{wfc} + S_{wft}$.

The volume fraction of the film subphase in the pores occupied by the connected nonwetting phase is assumed to be inversely proportional to the capillary pressure and is modeled by the power law

$$\frac{S_{wfc}}{S_{wfc} + S_{nc}} = A P_c^{-\alpha_{wf}}, \tag{25}$$

where A and $\alpha_{wf} > 0$ are fitting parameters and S_{nc} is the connected nonwetting-phase saturation. Differentiating with respect to t, it can be shown that

$$\frac{\partial S_{wfc}}{\partial t} = \frac{\kappa}{1-\kappa} \frac{\partial S_{nc}}{\partial t} - \alpha_{wf} A P_c^{-\alpha_{wf}-1} S_{nc} \frac{1+\kappa}{(1-\kappa)^2} \frac{\partial P_c}{\partial t}, \tag{26}$$

where $\kappa(P_c) = A P_c^{-\alpha_{wf}}$. The first term on the right-hand side corresponds to the change in S_{wfc} due to drainage (imbibition) of pores, as well as untrapping (trapping) of the nonwetting phase. This is the contribution to the volumetric transfer term $Q_{w_{bulk}-wf}$ arising from the transfer of S_{wfc} to $S_{w_{bulk}}$. The second term on the right-hand side corresponds to the shrinking (swelling) of the film subphase as the capillary pressure increases (decreases). Note that this term also corresponds to the term $\lambda_{wf} \frac{\partial S_w}{\partial S_t}$ in Eq. (23), which is the direct increase or decrease of the film subphase. Hence, we obtain an expression for $\lambda_{w_{film}}$:

$$\lambda_{w_{film}} = -\alpha_{wf} A P_c^{-\alpha_{wf}-1} S_{nc} \frac{1+\kappa}{(1-\kappa)^2} \frac{\partial P_c}{\partial S_w} \tag{27}$$

In order to model S_{wft}, imbibition and secondary drainage have to be distinguished ($S_{wft} = 0$ during primary

drainage). During imbibition, the change in S_{wft} is related to the capillary pressure at which trapping takes place, and can be written as

$$\frac{\partial S_{wft}^{imb}}{\partial t} = \frac{A P_c^{-\alpha_{wf}}}{1 - A P_c^{-\alpha_{wf}}} \frac{\partial S_{nt}}{\partial t}, \tag{28}$$

where S_{nt} is the trapped nonwetting-phase saturation. However, during secondary drainage, the change in S_{wft} due to untrapping is determined not by the capillary pressure at the time of trapping but that at the time at which trapping took place. This can be written as

$$\frac{\partial S_{wft}^{dr}}{\partial t} = \frac{A P_c^{imb}(S_{nt})^{-\alpha_{wf}}}{1 - A P_c^{imb}(S_{nt})^{-\alpha_{wf}}} \frac{\partial S_{nt}}{\partial t}. \tag{29}$$

where P_c^{imb} is the capillary pressure function for the imbibition preceding the secondary drainage but evaluated at the current S_{nt}. Summing Eqs. (26) and (28) for imbibition and (26) and (29) for drainage, one arrives at an expression for $Q_{w_{bulk}-wf}$ for imbibition and drainage:

$$Q_{w_{bulk}-wf}^{imb} = \frac{\kappa}{1-\kappa}\frac{\partial S_{nc}}{\partial t} + \frac{\kappa}{1-\kappa}\frac{\partial S_{nt}}{\partial t},$$

$$Q_{w_{bulk}-wf}^{dr} = \frac{\kappa}{1-\kappa}\frac{\partial S_{nc}}{\partial t} + \frac{A P_c^{imb}(S_{nt})^{-\alpha_{wf}}}{1 - A P_c^{imb}(S_{nt})^{-\alpha_{wf}}} \frac{\partial S_{nt}}{\partial t}.$$

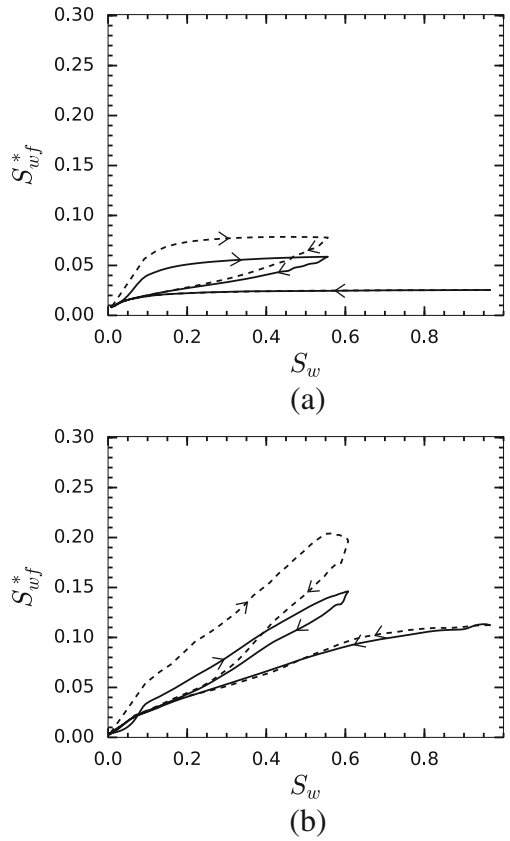

Fig. 11 Comparison between the $S^*_{wf} - S_w$ curves obtained from the model Eqs. (26–29) (*solid lines*) and from pore-network simulations (*dashed lines*). **a** For network B with calibrated parameters $A = 1.12 \cdot 10^5$ and $\alpha = 1.40$. **b** For network C with calibrated parameters $A = 126$ and $\alpha = 1.03$. The values used for P_c and S_{nt} are obtained from network simulations

Figure 11 shows the $S^*_{wf} - S_w$ relation as obtained from pore-network simulation data and by the calibrated model Eqs. (26–29) for networks B and C. As can be observed, there is excellent quantitative agreement for the primary drainage curves, which were used to calibrate the parameters A and α_{wf} in Eq. (25). There is poorer quantitative agreement for the secondary imbibition and secondary drainage curves. Better agreement may be obtained by using the SI and SD data in order to calibrate the parameters.

5 Discussions and conclusions

The pore-network study presented in Section 3 strongly suggests that the hysteresis in the wetting phase relative permeability is due to difference in the wetting corner film thickness between drainage and imbibition. Furthermore, the hysteresis trends presented here match two-phase experimental results reported in [1] and [33], where the wetting phase relative permeability is larger during imbibition than during drainage for a given wetting phase saturation. Based on observations from the network study, a model for the wetting phase relative permeability was proposed, with its independent variables being the bulk and film wetting subphases. The proposed model was shown to capture the hysteretic trends in the $S_w - k_{rw}$ relation.

However, the difference between advancing and receding contact angles (another possible cause for hysteresis), which occurs in realistic porous media, was not considered in the pore-network study presented here. In network models which capture contact angle hysteresis (e.g., [34]), film swelling is initially suppressed during imbibition and the contact angle in each pore is increased until the receding contact angle is reached. On reaching the receding contact angle, the film starts swelling. Taking this behavior into account can change both the volume of the wetting film phase as well as the sequence in which the individual pores are imbibed. This in turn would lead to changes in the observed $S_w - k_{rw}$ curves. In order to apply to more general cases, the proposed subphase evolution models would need to be extended to take these pore-scale mechanisms into account.

Analyzing the wetting subphases was important in understanding relative relative permeability hysteresis. A similar

analysis can be done on experimentally obtained data, if available. Note that such an analysis is not only relevant for modeling relative permeability hysteresis, but also has great value for modeling dispersion in two-phase flow through porous media. For example, it has been shown previously in [38] that taking film flow into account greatly affects the dispersion coefficient in the wetting phase.

Acknowledgments The authors would like to acknowledge Soheil Esmaeilzadeh for conducting preliminary pore-network simulations of the wetting subphase saturations during a semester project at ETH Zurich. The authors would also like to thank Total SA for financial support of this work.

References

1. Akbarabadi, M., Piri, M.: Relative permeability hysteresis and capillary trapping characteristics of supercritical co 2/brine systems: an experimental study at reservoir conditions. Adv. Water Resour. **52**, 190–206 (2013)
2. Arns, J.Y., Arns, C.H., Sheppard, A.P., Sok, R.M., Knackstedt, M.A., Pinczewski, W.V.: Relative permeability from tomographic images; effect of correlated heterogeneity. J. Pet. Sci. Eng. **39**(3), 247–259 (2003)
3. Arns, J.Y., Robins, V., Sheppard, A.P., Sok, R.M., Pinczewski, W., Knackstedt, M.A.: Effect of network topology on relative permeability. Transp. Porous Media **55**(1), 21–46 (2004)
4. Bakke, S., ØRen, P.: 3-d pore-scale modelling of sandstones and flow simulations in the pore networks. SPE J. **2**(2), 136–149 (1997)
5. Bear, J.: Dynamics of fluids in porous media. In: Dynamics of Fluids in Porous Media. American Elsevier (1967)
6. Bennion, B., Bachu, S., et al.: Relative permeability characteristics for supercritical Co2 displacing water in a variety of potential sequestration zones. In: SPE Annual Technical Conference and Exhibition. Society of Petroleum Engineers (2005)
7. Benson, S., Pini, R., Reynolds, C., Krevor, S.: Relative permeability analysis to describe multi-phase flow in co2 storage reservoirs Global CCS Institute (2013)
8. Berg, S., Armstrong, R., Georgiadis, A., Ott, H., Schwing, A., Neiteler, R., Brussee, N., Makurat, A., Rucker, M., Leu, L.: Onset of oil mobilization and nonwetting-phase cluster-size distribution. Petrophysics **56**(01), 15–22 (2015)
9. Blunt, M.J.: Effects of heterogeneity and wetting on relative permeability using pore level modeling. SPE J. **2**(01), 70–87 (1997)
10. Blunt, M.J.: Flow in porous media - pore-network models and multiphase flow. Current opinion in colloid & interface science **6**(3), 197–207 (2001)
11. Blunt, M.J., Jackson, M.D., Piri, M., Valvatne, P.H.: Detailed physics, predictive capabilities and macroscopic consequences for pore-network models of multiphase flow. Adv. Water Resour. **25**(8), 1069–1089 (2002)
12. Blunt, M.J., Jackson, M.D., Piri, M., Valvatne, P.H.: Detailed physics, predictive capabilities and macroscopic consequences for pore-network models of multiphase flow. Adv. Water Resour. **25**(8), 1069–1089 (2002)
13. Carlson, F.: Simulation of relative permeability hysteresis to the nonwetting phase. In: SPE Annual Technical Conference and Exhibition (1981)
14. Constantinides, G.N., Payatakes, A.C.: Network simulation of steady-state two-phase flow in consoliyeard porous media. AIChE J **42**(2), 369–382 (1996)
15. Dias, M.M., Payatakes, A.C.: Network models for two-phase flow in porous media part 1. Immiscible microdisplacement of non-wetting fluids. J. Fluid Mech. **164**, 305–336 (1986)
16. Fatt, I.: The network model of porous media (1956)
17. Gunstensen, A.K., Rothman, D.H.: Lattice-boltzmann studies of immiscible two-phase flow through porous media. Journal of Geophysical Research: Solid Earth **98**(B4), 6431–6441 (1993)
18. Herring, A.L., Harper, E.J., Andersson, L., Sheppard, A., Bay, B.K., Wildenschild, D.: Effect of fluid topology on residual nonwetting phase trapping: implications for geologic co 2 sequestration. Adv. Water Resour. **62**, 47–58 (2013)
19. Hilfer, R.: Macroscopic capillarity without a constitutive capillary pressure function. Physica A: Statistical Mechanics and its Applications **371**(2), 209–225 (2006)
20. Hilfer, R., ØRen, P.: Dimensional analysis of pore scale and field scale immiscible displacement. Transp. Porous Media **22**(1), 53–72 (1996)
21. Huang, H., Meakin, P., Liu, M.: Computer simulation of two-phase immiscible fluid motion in unsaturated complex fractures using a volume of fluid method. Water Resour. Res. 41(12) (2005)
22. Idowu, N.A., Blunt, M.J.: Pore-scale modelling of rate effects in waterflooding. Transp. Porous Media **83**(1), 151–169 (2010)
23. Jerauld, G., Salter, S.: The effect of pore-structure on hysteresis in relative permeability and capillary pressure: pore-level modeling. Transp. Porous Media **5**(2), 103–151 (1990)
24. Joekar-Niasar, V., Hassanizadeh, S., Dahle, H.: Non-equilibrium effects incapillarity and interfacial area in two-phase flow: dynamic pore-network modelling. J. Fluid Mech. **655**(1), 38–71 (2010)
25. Joekar-Niasar, V., Hassanizadeh, S.M.: Uniqueness of specific interfacial area–capillary pressure–saturation relationship under non-equilibrium conditions in two-phase porous media flow. Transp. Porous Media **94**(2), 465–486 (2012)
26. Khayrat, K.: Modeling hysteresis for two-phase flow in porous media: from micro to macro scale. Ph.D. thesis, Dissertation, ETH-zürich, 2016, Nr.23273 (2016)
27. Khayrat, K., Jenny, P.: Subphase approach to model hysteretic two-phase flow in porous media. Transp. Porous Media **111**(1), 1–25 (2016)
28. Killough, J.: Reservoir simulation with history-dependent saturation functions. Old SPE J **16**(1), 37–48 (1976)
29. Land, C.S.: Calculation of imbibition relative permeability for two-and three-phase flow from rock properties. Soc. Pet. Eng. J **8**(02), 149–156 (1968)
30. Lenormand, R., Zarcone, C., Sarr, A.: Mechanisms of the displacement of one fluid by another in a network of capillary ducts. J. Fluid Mech. **135**, 337–353 (1983)
31. Li, X., Zhang, Y., Wang, X., Ge, W.: Gpu-based numerical simulation of multi-phase flow in porous media using multiple-relaxation-time lattice boltzmann method. Chem. Eng. Sci. **102**, 209–219 (2013)
32. Moebius, F., Or, D.: Inertial forces affect fluid front displacement dynamics in a pore-throat network model. Phys. Rev. E. **90**(2), 023–019 (2014)
33. Oak, M., Baker, L., Thomas, D.: Three-phase relative permeability of berea sandstone. J. Petrol. Tech. **42**(08), 1–054 (1990)
34. Øren, P., Bakke, S., Arntzen, O.: Extending predictive capabilities to network models. SPE J **3**, 324–36 (1998)
35. Raeini, A.Q., Blunt, M.J., Bijeljic, B.: Direct simulations of two-phase flow on micro-ct images of porous media and upscaling of pore-scale forces. Adv. Water Resour. **74**, 116–126 (2014)
36. Ransohoff, T., Radke, C.: Laminar flow of a wetting liquid along the corners of a predominantly gas-occupied noncircular pore. J. Colloid Interface Sci. **121**(2), 392–401 (1988)

37. Reeves, P.C., Celia, M.A.: A functional relationship between capillary pressure, saturation, and interfacial area as revealed by a pore-scale network model. Water Resour. Res. **32**(8), 2345–2358 (1996)
38. Sahimi, M., Imdakm, A.: The effect of morphological disorder on hydrodynamic dispersion in flow through porous media. J. Phys. A Math. Gen. **21**(19), 3833 (1988)
39. Schlüter, S., Berg, S., Rücker, M., Armstrong, R., Vogel, H.J., Hilfer, R., Wildenschild, D.: Pore-scale displacement mechanisms as a source of hysteresis for two-phase flow in porous media. Water Resources Research (2016)
40. Singh, K., Bijeljic, B., Blunt, M.J.: Imaging of oil layers, curvature, and contact angle in a mixed-wet and a water-wet carbonate rock. Water Resources Research (2016)
41. Tokunaga, T.K.: Physicochemical controls on adsorbed water film thickness in unsaturated geological media. Water Resour. Res. 47(8) (2011)
42. Tomin, P., Lunati, I.: Hybrid multiscale finite volume method for two-phase flow in porous media. J. Comput. Phys. **250**, 293–307 (2013)
43. Tsakiroglou, C., Aggelopoulos, C., Terzi, K., Avraam, D., Valavanides, M.: Steady-state two-phase relative permeability functions of porous media: a revisit. Int. J. Multiphase Flow **73**, 34–42 (2015)
44. Wilkinson, D., Willemsen, J.F.: Invasion percolation: a new form of percolation theory. J. Phys. A Math. Gen. **16**(14), 3365 (1983)